Method for Estimating Locations of Laser-Induced Stray Charges on Surface-Electrode Ion Traps Using Secular Frequency Shift at Multiple Ion Positions

Changhyun Jung,[1,2,3] Junho Jeong,[1,2,3] Seungwoo Yoo,[2,3,4,5] Taehyun Kim,[2,3,4,5] and Dongil "Dan" Cho[1,2,3,*]

[1] *Department of Electrical and Computer Engineering, Seoul National University, Seoul 08826, Republic of Korea*
[2] *Automation and System Research Institute, Seoul National University, Seoul 08826, Republic of Korea*
[3] *Inter-university Semiconductor Research Center, Seoul National University, Seoul 08826, Republic of Korea*
[4] *Department of Computer Science and Engineering, Seoul National University, Seoul 08826, Republic of Korea*
[5] *Institute of Computer Technology, Seoul National University, Seoul 08826, Republic of Korea*

(Received 13 December 2022; revised 19 May 2023; accepted 21 June 2023; published 17 July 2023)

This paper develops a method for estimating the locations of laser-induced stray charges on surface-electrode ion traps. How the electric potential at the trapped-ion location changes in the presence of laser-induced stray charges is theoretically modeled, and the magnitude of the shift in the secular frequency of a trapped ion is derived from the model. This model can be used inversely to find the locations of stray charges from the secular frequency shift under certain conditions. Typically, this inverse relationship is not unique. However, in surface-electrode ion traps, the secular frequency shift caused by the stray charges can be measured at multiple ion positions, and therefore, the required number of secular-frequency-shift measurements can be performed to determine the stray-charge locations uniquely. This model is experimentally evaluated by intentionally producing electric charges at a single location by irradiating a laser onto that spot and by measuring the resulting secular frequency shift. The location of produced charges is estimated from the measured result, and the estimated location is consistent with where the laser is irradiating. The developed method can be applied to characterize the laser-induced stray charges, which in turn can be used to design experiments to avoid or reduce the occurrence of stray charges.

DOI: 10.1103/PhysRevApplied.20.014032

I. INTRODUCTION

The development of a universal quantum computer based on surface-electrode ion traps has been actively conducted in recent years [1–3]. The surface-electrode ion traps have the advantages of reproducibility and scalability [4–7], which can be achieved by using ion shuttling among multiple trapping regions [8,9]. Also, the surface-electrode ion traps allow the integration of optical components [10,11] and electrical elements [12–14]. However, even small variations in surrounding electric fields can cause the micromotion of trapped ions [15,16], and therefore, stray electric fields at the ion location can cause the uncertainty of quantum gate operations using the trapped ions [17,18]. Especially in surface-electrode ion traps, the distance between the trapped ions and the nearest electrode is typically smaller than that of macroscopic ion traps, and thus, the effect of stray electric fields on the trapped ions is considered to be a severe problem [19,20]. To date, various methods have been developed only for detecting and canceling stray electric fields at the ion location [21–24]. In other words, all of these methods focus on the suppression of the problem by applying additional electric fields, and therefore, the root cause of the problem cannot be identified [5,15].

A laser-induced stray charge is one of the causes of induced stray electric fields at the ion location and is generated when photoelectrons emitted from electrode surfaces are accumulated in nearby dielectric surfaces [25–27] or when electrons are ejected from the antireflection coating of the glass substrate [25]. The laser-induced stray charge is time dependent [5,28], and therefore, it is challenging to maintain the stability of trapped ions for a long time by canceling only the resulting stray electric fields observed once in the past. Periodical compensation for stray electric fields must be used to reproduce identical measurement results over a long period of time. Also, the accumulation rate at which the laser-induced stray charges occur depends on the incident laser frequency [26]. Since most ions employed in ion traps utilize high-frequency lasers [29,30], there is always the possibility of photoelectrons being emitted from the trap surface [31–33]. When stray

*dicho@snu.ac.kr

electric fields from the laser-induced stray charges become problematic, they are suppressed by adjusting the laser propagation paths until the stray electric fields appear to be minimized using trial and error because the locations of stray charges are unknown [21,34].

Here, a method for estimating the locations of laser-induced stray charges on surface-electrode ion traps is developed. The change in the electric potential at the trapped-ion location is modeled in the presence of a laser-induced stray charge, and the resulting shift in the secular frequency of a trapped ion is analyzed. The location of the stray charge is then estimated from the secular frequency shift. In the estimation process, it is assumed that the secular frequency can be measured at multiple ion positions in surface-electrode ion traps, and therefore, the required number of secular-frequency-shift measurements can be performed to uniquely determine the stray-charge location. This model is extended to the case where laser-induced stray charges occur at multiple locations. Various test data are generated by assuming multiple stray charges at random locations, and the locations of multiple stray charges are estimated from the secular frequency shift observed in the test data. The estimated locations are compared with the actual locations used to generate the test data. The number of stray-charge locations that can be distinguished using the developed method is also analyzed in this process. To support the effectiveness of the developed method, a computer simulation is performed for situations in which stray charges occur at various locations, and the resulting secular frequency shift is observed at multiple ion positions. The locations of stray charges are then estimated from the frequency shift observed in the simulation result. Also, the developed method is experimentally evaluated by intentionally producing electric charges at a single location by irradiating a laser onto that spot, and by measuring the resulting secular frequency shift. The location of produced charges is estimated from the measured secular frequency shift, and the estimated location agrees with the laser-irradiation region identified from charge-coupled device (CCD) images within the margin of error.

II. THEORETICAL MODEL

The following discussion assumes a Paul trap, which confines charged particles in space using an oscillating electric field and an electrostatic field [35]. Figure 1 shows a schematic of a surface-electrode ion trap. The surface-electrode ion trap typically has radio-frequency (rf) electrodes and inner or outer direct current (dc) electrodes in a plane, and to measure the secular frequency at various ion positions (z_{ion}), the proposed method moves the trapped ions along the longitudinal direction of the rf electrodes (z axis in Fig. 1).

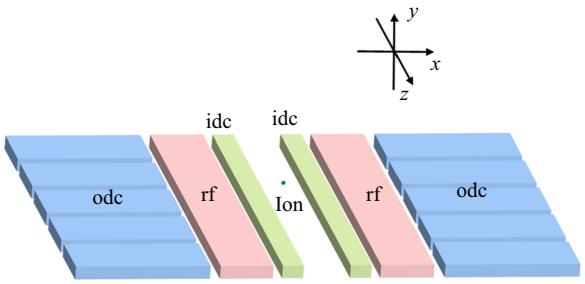

FIG. 1. Schematic of a surface-electrode ion trap. Green dot, rf, odc, and idc indicate a single trapped ion, rf electrodes, segmented outer dc electrodes, and inner dc electrodes, respectively.

A. Model for a single stray-charge location

When the trap center is positioned at $(0, 0, z_{\mathrm{ion}})$, the electric potential experienced by an ion consists of a time-dependent part that varies sinusoidally at the rf drive frequency, ω_{rf}, and a time-independent electrostatic part, as follows [36]:

$$\begin{aligned}\Phi_0(x,y,z,t) = &\frac{1}{2}U_0[ax^2 + by^2 + c(z - z_{\mathrm{ion}})^2] \\ &+ \frac{1}{2}V_0\cos(\omega_{\mathrm{rf}}t)[a'x^2 + b'y^2 \\ &+ c'(z - z_{\mathrm{ion}})^2],\end{aligned} \tag{1}$$

where U_0 and V_0 are the electrostatic potential and the rf drive voltage, respectively. To satisfy the Laplace equation at any moment in time, the relationships among the constants are

$$a + b + c = a' + b' + c' = 0. \tag{2}$$

Additionally, for a linear trap, $c' = 0$ is assumed to be similar to that reported in Ref. [36]. The equation of motion of a single trapped ion oscillating along the z direction at Φ_0 can be then written as

$$\ddot{z} = -\frac{1}{m} \times \frac{\partial}{\partial z}(Z|e|\Phi_0) = -\frac{Z|e|}{m}U_0 c(z - z_{\mathrm{ion}}), \tag{3}$$

where $Z|e|$ and m are the electric charge and the mass of the ion, respectively. Equation (3) describes the harmonic oscillation of a particle along the z axis, and the corresponding secular frequency ($\omega_{z0}(z_{\mathrm{ion}})$) can be written as

$$\omega_{z0}(z_{\mathrm{ion}}) = \sqrt{\frac{Z|e|}{m} \times \frac{\partial^2\Phi_0}{\partial z^2}}\Bigg|_{z=z_{\mathrm{ion}}}. \tag{4}$$

Let Φ_q be the potential generated by a laser-induced stray charge (Q) when the stray charge is generated in

the vicinity of the trapped ion. Then, the resulting secular frequency (ω_z) can be written as

$$\omega_z(z_{\rm ion}) = \sqrt{\frac{Z|e|}{m}\left(\frac{\partial^2\Phi_0}{\partial z^2}+\frac{\partial^2\Phi_q}{\partial z^2}\right)}\Bigg|_{z=z_{\rm ion}}. \quad (5)$$

In typical cases where $(\partial^2\Phi_q/\partial z^2) \ll (\partial^2\Phi_0/\partial z^2)$, Eq. (5) can be rewritten using the Taylor expansion as

$$\omega_z(z_{\rm ion}) \cong \omega_{z0}(z)\left[1+\frac{\partial^2\Phi_q}{2\partial z^2}\left(\frac{\partial^2\Phi_0}{\partial z^2}\right)^{-1}\right]\Bigg|_{z=z_{\rm ion}}. \quad (6)$$

Since the secular frequency shift in the z axis ($\Delta\omega_z$) is $\omega_z - \omega_{z0}$, $\Delta\omega_z$ can be rewritten as

$$\Delta\omega_z(z_{\rm ion}) \cong \frac{Z|e|}{2m\omega_{z0}(z)} \times \frac{\partial^2\Phi_q}{\partial z^2}\Bigg|_{z=z_{\rm ion}}. \quad (7)$$

Let charge Q be locally induced at (x_q, y_q, z_q) [25], and let $x_{\rm ion}$, $y_{\rm ion}$, and $z_{\rm ion}$ be the coordinates of the ion. $\Delta\omega_z$ can then be written as

$$\Delta\omega_z(x_{\rm ion}, y_{\rm ion}, z_{\rm ion}) \cong \frac{KQ(x_d^2+y_d^2-2z_d^2)}{\omega_{z0}(z_{\rm ion})(x_d^2+y_d^2+z_d^2)^{5/2}}, \quad (8)$$

where K is $-(Z|e|/8\pi\varepsilon_0 m)$, and x_d, y_d, and z_d indicate $(x_{\rm ion}-x_q)$, $(y_{\rm ion}-y_q)$, and $(z_{\rm ion}-z_q)$, respectively. According to Eq. (8), when $z_d^2 < (1/2)(x_d^2+y_d^2)$, the sign of $\Delta\omega_z$ is determined by the sign of Q. Conversely, when $z_d^2 \gg (1/2)(x_d^2+y_d^2)$, $\Delta\omega_z$ converges to zero. Thus, in principle, the single stray-charge location (x_q, y_q, z_q) can be estimated by fitting Eq. (8) to the measured $\Delta\omega_z(z_{\rm ion})$.

B. Assumption

Constraints that can uniquely determine the location of stray charges from $\Delta\omega_z(z_{\rm ion})$ measured at multiple ion positions $(0, 0, z_{\rm ion})$ are considered, since various combinations of stray-charge locations and other causes can result in similar distributions of $\Delta\omega_z(z_{\rm ion})$. First, it is assumed that the secular frequency is changed only by laser-induced stray charges, and other factors are negligible [15]. Also, only stray charges in the vicinity of the ion position can shift the secular frequency of the trapped ion, and the influence of other stray charges sufficiently far away from the ion position is negligible. This assumption can also be inferred from Eq. (8) that the frequency shift due to stray charges far from the ion position converges to zero. It is also assumed that the location of laser-induced stray charge does not change with time. Considering only the case where the stray charges occur on the trap surface, the magnitude of $|y_{\rm ion}-y_q|$ is set to be equal to the ion height. In addition, it is assumed that Φ_0 has the same curvature $(\partial^2\Phi_0/\partial z^2|_{z_{\rm ion}} = c)$ independent of $z_{\rm ion}$, and $\omega_{z0}(z_{\rm ion})$ is fixed. During curve fitting, x_q, z_q, and Q are used as free parameters.

C. Model for multiple stray-charge locations

In this section, the model discussed in Sec. II A is extended to the case where stray charges occur at multiple locations in the vicinity of the trapped ion. In this case, the electric potential generated by multiple Q_m is equal to the sum of $\Phi_{q,m}$ by each Q_m. When $(\partial^2\Phi_{q,m}/\partial z^2) \ll (\partial^2\Phi_0/\partial z^2)$, $\Delta\omega_z$ can be approximated as

$$\Delta\omega_z(x_{\rm ion}, y_{\rm ion}, z_{\rm ion}) \cong \frac{K}{\omega_{z0}(z_{\rm ion})} \times \sum_{m=1}^{n}\frac{Q_m(x_{d,m}^2+y_{d,m}^2-2z_{d,m}^2)}{(x_{d,m}^2+y_{d,m}^2+z_{d,m}^2)^{5/2}}, \quad (9)$$

where Q_m indicates the mth stray charge induced at $(x_{q,m}, y_{q,m}, z_{q,m})$, and $x_{d,m}$, $y_{d,m}$, and $z_{d,m}$ are $(x_{\rm ion}-x_{q,m})$, $(y_{\rm ion}-y_{q,m})$, and $(z_{\rm ion}-z_{q,m})$, respectively. In subsequent sections, note that the initial secular frequency on the z axis is kept constant at a value of $2\pi \times 250$ kHz. This frequency is obtained from the simulation when the dc voltages utilized in the experiment are applied. The ion height is also fixed to 108 μm, which corresponds to the ion height of the trap used in the experiment. Additionally, a loading slot with a width of 80 μm is considered, resulting in a distance of approximately 115 μm between the ion and the nearest electrode. Also, the trapping of $^{174}Yb^+$ ions is taken into consideration.

When different stray charges are sufficiently far apart, the number of observed peaks in the plot of $\Delta\omega_z(z_{\rm ion})$ can be equal to the number of charge locations, as illustrated in Fig. 2(a). In this case, the locations of different charges can be easily estimated from each peak in the $\Delta\omega_z(z_{\rm ion})$ plot. However, when different charges are closely located, only a single $\Delta\omega_z(z_{\rm ion})$ peak can be observed, as shown in Fig. 2(b). In this case, it is challenging to distinguish the locations of different charges. However, the proposed method can still work to some degree. Thus, to figure out the number of stray-charge locations that can be distinguished using the developed method when there is only a single dominant peak in the $\Delta\omega_z(z_{\rm ion})$ plot, we try to fit the curve of Eq. (9) to numerous test data generated with the assumption of multiple stray charges at random locations. Note that all curve-fitting processes are performed using the SciPy library [37]. The curve-fitting algorithm is based on the least-squares method, which is aimed at approximating the locations of stray charges. Specifically, the Levenberg-Marquardt method is utilized for the approximation. Estimated Q_m, $x_{q,m}$, and $z_{q,m}$ in the curve-fitting processes are then compared with the actual Q_m, $x_{q,m}$, and $z_{q,m}$ used for the generation of test data. To quantify the effectiveness of the fitting for numerous test data, the errors between the estimated values and the actual values are defined as the maximum value among the fractional errors of fitted parameters, such as Q_1, $x_{q,1}$, $z_{q,1}$, ..., Q_n,

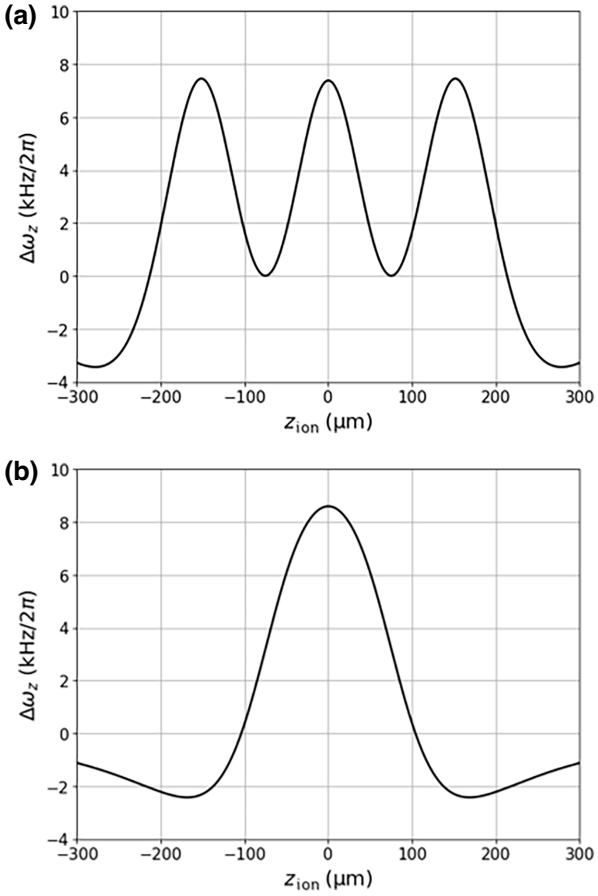

FIG. 2. Calculation results of $\Delta\omega_z(z_{\text{ion}})$ when charges occur at three separate locations. (a) Calculation result of three $\Delta\omega_z$ peaks caused by three stray charges that are sufficiently far apart. Different stray charges are separated by 150 μm on the z axis. (b) Calculation result of a single $\Delta\omega_z$ peak due to three stray charges close enough for each peak to overlap. Different stray charges are separated by 50 μm on the z axis.

$x_{q,n}$, $z_{q,n}$. Depending on the number of charge locations from 1 to 5, the average error rates are 0.0%, (0.3 ± 0.7)%, (3.3 ± 4.4)%, (13.3 ± 12.9)%, and (24.2 ± 13.5)%, respectively, as illustrated in Fig. 3. Note that the minimum distance between different charges is 10 μm in the test data. The increase in error rates with the number of stray-charge locations can be attributed to the increase in the number of free parameters. For instance, when the number of stray-charge locations is 4, the number of free parameters that need to be determined increases to 12. Also, the large error range observed when the number of stray charges is 4 or more is mainly due to the presence of outliers, which occur when different charges are located close to each other at a distance of 10 μm. Furthermore, the curve-fitting process often fails when the number of charge locations is four or more. Thus, it is concluded that, in cases where there is a single dominant $\Delta\omega_z$ peak, up to 3 stray-charge locations can be identified, as long as different charges are separated

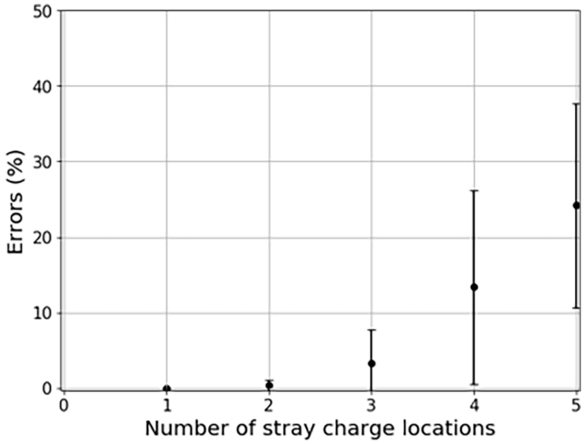

FIG. 3. Estimated errors between actual and estimated values for the number of stray-charge locations. When the number of stray-charge locations ranges from 1 to 5, estimated average errors are 0.0%, (0.3 ± 0.7)%, (3.3 ± 4.4)%, (13.3 ± 12.9)%, and 24.2 ± 13.5%, respectively. Error bars indicate standard deviations.

by more than 10 μm, which is smaller than the typical size of beam waist used in ion traps.

In typical cases, the curve-fitting process must be performed without knowing the number of stray-charge locations. Therefore, during the curve-fitting process, we vary the number of free parameters necessary for multiple charge locations. When the number of free parameters is larger than the necessary free parameters, $Q_m = 0$ for some parameters is obtained, or the total charge at a single location is divided into two charges located at the same position. Conversely, when the number of free parameters is less than the minimum number to describe the actual situation, incorrect $x_{q,m}$ and $z_{q,m}$ are obtained. In this case, as the number of free parameters increases, completely different fitting results are obtained until the minimum number of free parameters is reached. Consistent results are then obtained once a sufficient number of free parameters are used.

III. SIMULATION RESULTS

The calculation results of Eq. (9) are compared with the simulation results to support the effectiveness of the above model. Considering that the trapped ion moves only along the z axis, x_{ion} and y_{ion} are set to zero in Eq. (9). Φ_0 is obtained from a COMSOL Multiphysics simulation, and ω_{z0} is estimated from simulated Φ_0 using Eq. (4). A point charge is added to the simulation to produce the effect of the stray charge. Φ_q is obtained from the potential generated by the point charge. ω_z is calculated from simulated $\Phi_0 + \Phi_q$, and $\Delta\omega_z$ is obtained from the difference between ω_z and ω_{z0}. To simulate ion-position changes, the distance between the trap center and the point charge is varied in 40-μm increments over a range from -240 to $+240$ μm.

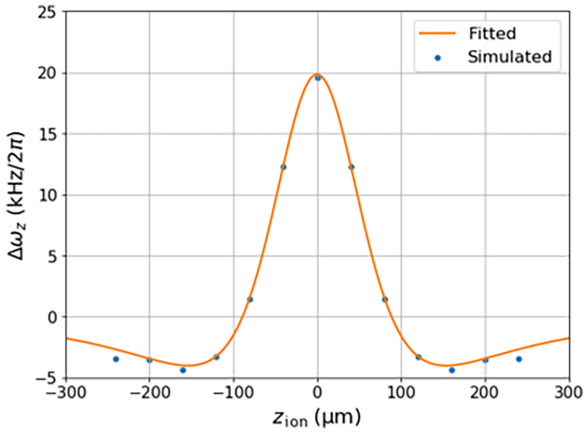

FIG. 4. Curve fitting and simulation results of $\Delta\omega_z$ as a function of z_{ion}. Orange line and blue dots indicate the fitting result and simulation result, respectively. Simulation result shows simulated $\Delta\omega_z$ when z_{ion} changes by 40 μm in the range from −240 to +240 μm. Fitted result indicates the curve-fitting result of Eq. (9) to the simulation result.

Figure 4 shows the simulation and curve-fitting results of $\Delta\omega_z$ caused by a single charge. The charge amount is set to be $-1000e$, where e is the elementary charge. The simulated point charge is positioned at (55, −108, 0) μm, assuming that the stray charge is located on an inner dc electrode. The estimated $\Delta\omega_z$ in the simulation is shown as the blue dots in Fig. 4. A single dominant peak in the $\Delta\omega_z$ plot is observed at $z_{\text{ion}} = 0$. The curve-fitting result of Eq. (9) to the simulated $\Delta\omega_z$ is illustrated as the orange line in Fig. 4. Estimated x_q and z_q are 64 and 0 μm, respectively, and Q is obtained as $-979e$. It is also confirmed that the fitting results of x_q and z_q are the same even when the number of charge locations (n) in Eq. (9) is increased to three. Thus, the number of charge locations is inferred to be one. There is a discrepancy between the fitting and simulation results that may be attributed to errors resulting from the use of a first-order approximation in the theoretical model or from inaccuracies in the simulation itself.

Figure 5(a) shows the simulation result for two charges that are far apart (approximately 160 μm), and both charges are assumed to have an amount of $-1000e$. In this case, one of the point charges is set to be located at −80 μm, and the other is set to be located at 80 μm along the z axis, while $x_{q,m}$ and $y_{q,m}$ are the same. When n is set to 1 during a curve fitting to Eq. (9), only a single peak at $z_{\text{ion}} = 0$ is observed. However, when n in Eq. (9) is 2 or more, two $\Delta\omega_z$ peaks located at two different positions are observed, as illustrated by the orange line in Fig. 5(a). The estimated $z_{q,1}$ and $z_{q,2}$ are ±80 μm, and both $x_{q,1}$ and $x_{q,2}$ are estimated to be 65 μm. Additionally, the estimated amount of both charges is $-1028e$. Thus, the number of charge locations can be inferred to be two. The results agree with the actual values regarding the coordinates and number of charge locations.

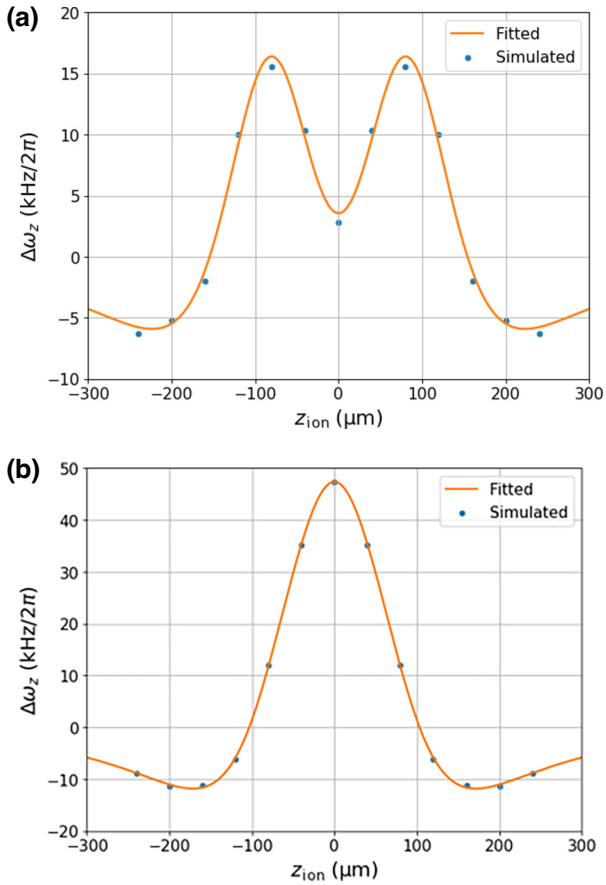

FIG. 5. Curve fitting and simulation results of $\Delta\omega_z$ by multiple stray charges. (a) Simulation result of $\Delta\omega_z$ when two stray charges are far apart, and the distance between the two charges is approximately 160 μm. Fitted result shows the curve-fitting result to the simulation result. (b) Simulation result of $\Delta\omega_z$ when three stray charges are close together, and $z_{q,m}$ of the three charges are −40, 0, and 40 μm, respectively. $x_{q,m}$ and $y_{q,m}$ are the same.

The simulation result for three charges that are close together is shown in Fig. 5(b). $z_{q,1}$, $z_{q,2}$, and $z_{q,3}$ are −40, 0, and 40 μm, respectively, and $x_{q,m}$ and $y_{q,m}$ are the same. All the charges are assumed to have an amount of $-1000e$. In this case, only a single peak is observed in the $\Delta\omega_z$ plot, as shown by the blue dots in Fig. 5(b). When n is one in Eq. (9), a plot similar to the shape of blue dots is drawn, and the z coordinate of the peak is zero. Also, when n is 2 in Eq. (9), a graph similar to the distribution of blue dots is observed, and the estimated values of $z_{q,1}$ and $z_{q,2}$ are ±34 μm. However, when n is 3 or more, three different z coordinates (0 and ±44 μm) are obtained while still observing a single peak, as illustrated by the orange line in Fig. 5(b). The estimated values for $x_{q,1}$, $x_{q,2}$, and $x_{q,3}$ are the same, at 60 μm, with estimated charge amounts of $-892e$ for the charge at $z_{\text{ion}} = 0$ and $-1072e$ for the charges at $z_{\text{ion}} = \pm 44$ μm. From these observations, it can

be concluded that there are three distinct charge locations, consistent with the coordinates of actual charge locations.

IV. EXPERIMENTAL RESULTS AND DISCUSSION

A surface-electrode ion trap with aluminum-copper alloy (1 wt %) electrodes is used in this experiment. The width of the loading slot, inner dc electrodes, rf electrodes, and the gap between electrodes are 80, 37, 75, and 8 μm, respectively, to confine the ions approximately 108 μm above the surface-electrode ion trap. The 32 pairs of segmented outer dc electrodes are included to displace the trapped ion. The surface-electrode ion trap is loaded in a vacuum chamber at room temperature, and the rf drive frequency is approximately $2\pi \times 32.42$ MHz. All experiments are performed with $^{174}Yb^{+}$ ions [34].

A laser with a wavelength of 399 nm, the second-shortest-wavelength laser among the lasers for trapping $^{174}Yb^{+}$ ions, is used to produce electric charges in a random area on the trap surface. Note that the photon energy of the 399-nm laser is approximately 3.1 eV, which may not be high enough to directly photoemit electrons from the electrode. However, as reported in Ref. [38], photoemission can occur in oxidized aluminum with a photon energy as low as 3.0 eV. The thickness of the native oxide layer or the potential applied to the electrode may affect the photoinduced process. The laser propagation direction is perpendicular to the trap surface (y direction in Fig. 1). A lens is added to the laser-propagation path to irradiate the surface of the trap with the laser locally. The secular frequency shift caused by the produced charges is estimated from the difference in the measured secular frequencies before and after shining the laser.

In subsequent experiments, a charging phenomenon is assumed as a model for the photoelectric effect on a metal surface modified with a thin insulating film, as previously presented in Ref. [26]. According to this model, when photoelectrons get trapped in the native oxide layer, the electrons form electron-hole pairs with the image charge in the electrode, which in turn may generate an electric field in the form of a dipole [25]. The rate at which charging occurs can be described by a rate equation as

$$\dot{Q} = \alpha - (\delta + \gamma)Q, \tag{10}$$

where α indicates the rate at which the incident laser accumulates new charges, δ is a constant for the screening effect by existing Q, and γ is a constant for the rate at which the accumulated charges are dissipated [26].

To change the ion position along the z axis, dc voltages applied to the segmented outer dc electrodes are adjusted. The dc voltages are numerically simulated to make both the secular frequency and ion height uniform at any ion position. Even when the estimated dc voltages are applied, micromotion may occur due to simulation errors. Slight adjustments of the dc voltages compensate for the micromotion, and then the secular frequency is measured using the parametric excitation method [39]. Amplitude modulation of the rf drive voltage is carried out by combining two rf signals of different frequencies to implement the parametric excitation. The initial secular frequencies along two radial directions are obtained as approximately $2\pi \times (820, 960)$ kHz.

A. Measurement results of $\Delta\omega_z$ by laser-induced charges

To find out experimentally whether $\Delta\omega_z$ can be caused by laser-induced stray charges, the secular frequency is measured before and after irradiating the surface of the trap with the laser. The beam radius and power of the laser are 2 μm and 20 μW, respectively. To measure the secular frequency once per minute, the interval of modulation frequency is set to 0.1 kHz, and the scan range is set to 10 kHz. The secular frequency is identified from the downward peak observed in the result of collecting the photons emitted from the trapped ion as a function of the modulation frequency. The blue, orange, and green lines in Fig. 6(a) show the measurement results of secular frequency before and after charging and after charge dissipation, respectively. The measured frequencies before and after shining the laser and after charge dissipation are $2\pi \times (267.88,\ 273.44, 267.75)$ kHz, respectively. The shift in the secular frequency is approximately $2\pi \times 5.56$ kHz after laser irradiation, and this indicates that the sign of Q is negative, according to Eq. (8).

The measurement results of secular frequency over time are shown in Fig. 6(b). The time in Fig. 6(b) indicates the time after starting to measure the first secular frequency. The secular frequency is measured over a period of 10 min. First, the secular frequency is measured with the charging laser turned *off* for the initial 2 min. Next, the secular frequency is observed for the following 5 min, while the charging laser is turned *on*, and then the laser irradiation is blocked to dissipate the existing charge. $\Delta\omega_z$ is estimated from the difference between the measured secular frequency before and after laser irradiation, and the errors are obtained from the standard deviation of the measured secular frequency after shining the laser. As shown in Fig. 6(b), the measured secular frequency is uniform before the laser is turned *on*. This indicates that $\Delta\omega_z$ depends only on the charging laser and other factors are negligible. Since the measured secular frequency at 3 min is almost uniform until 7 min, charge generation is inferred to saturate within 1 min. The secular frequency returns close to its original value within 1 min after laser irradiation is blocked. This result is different than the time constants of $t_1 = 78$ and $t_2 = 650$ s measured in another study using aluminum electrodes [31]. The 399-nm laser may have a fast dissipation rate due to its low photon energy, which can lead

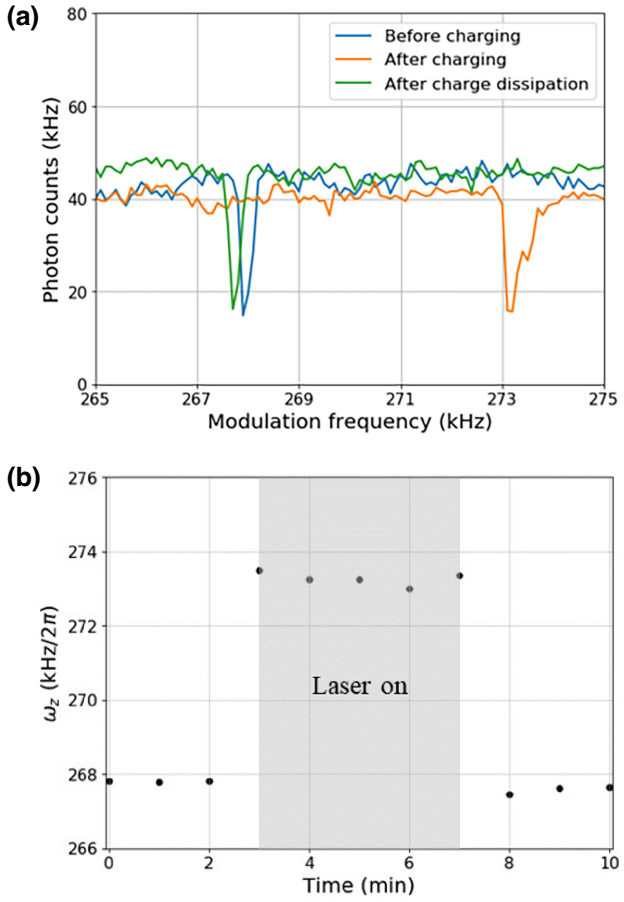

FIG. 6. Measurement results of secular frequency before and after shining the charging laser and after charge dissipation. (a) Collection results of the number of photons emitted from the trapped ion as a function of modulation frequency. Blue, orange, and green lines show the results before and after charging and after charge dissipation, respectively. Downward peaks indicate the secular frequency. Observed frequency before charging is approximately $2\pi \times 267.88$ kHz, whereas observed frequency after charging is approximately $2\pi \times 273.44$ kHz. Secular frequency returns close to its original value after the charge dissipates. (b) Measurement result of secular frequency (ω_z) over time. Gray box indicates the time of shining the charging laser. ω_z is uniform from 0 to 2 min and increases in the gray box. When laser irradiation is blocked, ω_z returns close to its original value.

to the photoelectrons being shallowly trapped in the native oxide layer (see Appendix A for additional details). Alternatively, the native oxide layer in our trap may be thinner than that in the previous study.

B. Location estimation of laser-induced charges

$\Delta\omega_z$ is obtained while changing z_{ion} by approximately 20 μm. The distance over which z_{ion} changes is estimated from CCD images. For each ion position, the initial secular frequency is measured, and then the process of shining the charging laser and measuring the secular frequency shift is performed. As shown by the blue dots in Fig. 7(a), $\Delta\omega_z$ is estimated to have the largest value of approximately $2\pi \times 6.52$ kHz near $z_{\text{ion}} = -20$ μm, and measured $\Delta\omega_z$ decreases as z_{ion} moves away from $z_{\text{ion}} = -20$ μm. Curve fitting is performed based on the measurement result of $\Delta\omega_z$ as a function of z_{ion}. Since only z_{ion} changes, both x_{ion} and y_{ion} are set to zero in Eq. (9). Considering the possibility that stray charges can occur at multiple locations, curve fitting is performed when n in Eq. (9) is from 1 to 3. From the results of curve fitting, only one set of $|x_q|$ and z_q is obtained uniformly, regardless of n, and only the estimated amount of the charge decreases when n increases. Thus, the number of charge locations is inferred to be one. $|x_q|$ and z_q are estimated to be (47 ± 26) and (-25 ± 11) μm, respectively, and Q is obtained as $(-277 \pm 64)e$. Note that only the magnitude of x_q can be obtained by analyzing $\Delta\omega_z$ as a function of z_{ion}, according to Eq. (9).

To determine the sign of x_q, $\Delta\omega_z$ is observed while changing x_{ion} by approximately 1.7 μm in the range from -5 to $+5$ μm. Note that the micromotion of the trapped ion is severe when the ion moves more than 5 μm away along the x axis, and therefore, changing x_{ion} is performed up to 5 μm. As can be seen through the blue dots in Fig. 7(b), measured $\Delta\omega_z$ is largest near $x_{\text{ion}} = -5$ μm and gradually decreases along x_{ion}. The orange line shows the calculation result using Eq. (9) when y_{ion} and z_{ion} are zero. The values of x_q, z_q, and Q are set to -47 μm, -25 μm, and $-277e$, respectively, according to the estimated results of $\Delta\omega_z$ as a function of z_{ion}. The sign of x_q is inferred to be $(-)$, since the measured $\Delta\omega_z$ decreases along with x_{ion}, and the plot of measured $\Delta\omega_z$ is comparable to the calculated $\Delta\omega_z$. Note that when the sign of x_q is opposite, the plot is flipped along the y axis.

C. Location analyses of laser-induced charges

The estimated location of the produced charge is compared with where the laser is irradiating. Figure 8 shows a CCD image of the surface-electrode ion trap and laser-irradiation regions. The laser-irradiation regions are identified from the laser spot that appears on the trap surface when the charging laser is blocked or not. Marks 1, 2, and 3 indicate the regions where the laser spot is observed. Among the marks, mark 1 is the region where the analyses in Secs. IV A and B are performed, and the coordinates are $x = (-51 \pm 6)$ μm and $z = (-23 \pm 5)$ μm relative to the initial ion position indicated by the green dot in Fig. 8. The result shows that the estimated coordinates of the produced charge are consistent with the coordinates of the laser-irradiation region within the margin of error.

The same experiments are repeated twice more by changing the laser-irradiation region. The investigation is repeated while irradiating the surface of the trap with the charging laser on marks 2 and 3 in Fig. 8, and the corresponding results are summarized as cases 2 and 3 in Table

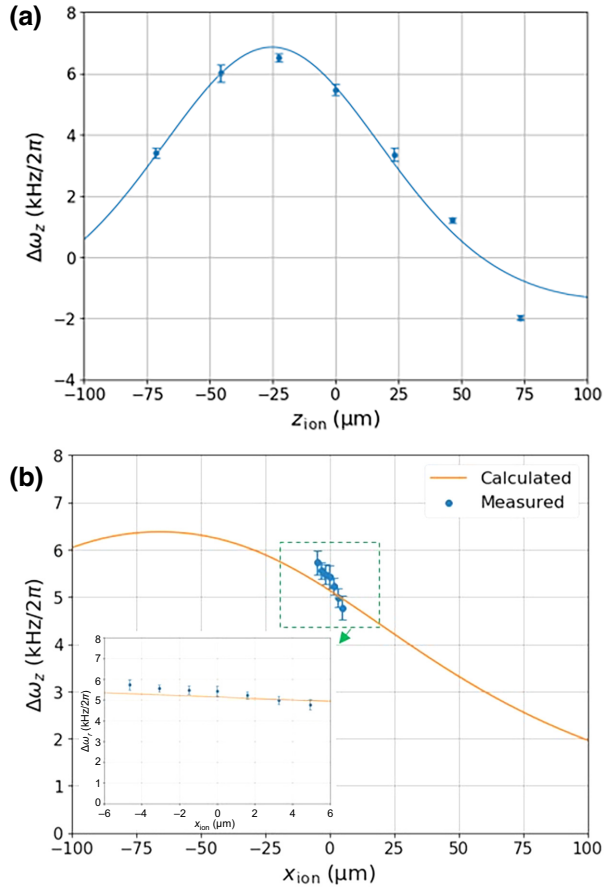

FIG. 7. Measurement results of $\Delta\omega_z$ as a function of ion position. (a) Measurement result of $\Delta\omega_z$ as a function of z_{ion}. When the ion is located near $z_{\text{ion}} = -20$ μm, $\Delta\omega_z$ is obtained as the largest value of approximately $2\pi \times 6.52$ kHz, and measured $\Delta\omega_z$ decreases as the ion moves away from $z_{\text{ion}} = -20$ μm. Based on the measurement result, estimated $|x_q|$, z_q, and Q are 47 μm, −25 μm, and $-277e$, respectively. (b) Measurement and calculation results of $\Delta\omega_z$ as a function of x_{ion}. Blue dots and orange line show the measured result and calculated result of Eq. (9), respectively. Interval between blue dots is approximately 1.7 μm, and measurement is performed in the range from −5 to +5 μm along the x axis. Orange line is drawn using $|x_q|$, z_q, and Q estimated from (a). Since measured $\Delta\omega_z$ decreases along x_{ion}, the sign of x_q is inferred to be (−). Inset shows the magnified plot in the range from −6 to +6 μm. Error bars indicate standard deviations.

I. The sign of z_q in case 2 and x_q in case 3 is intentionally set to be opposite from that in case 1 to validate that the sign of coordinates can be correctly identified. When case 1 and case 2 are compared, the sign can be distinguished even when the sign of z_q is opposite, and the magnitude of z_q can also be correctly estimated within the margin of error. Comparing case 1 and case 3, it is correctly distinguished that the sign of x_q is opposite. The magnitude of x_q is also correctly estimated within the margin of error. Note that the accuracy of the estimated amounts cannot be analyzed, since theoretical indicators that can compare the amount of produced charges do not exist.

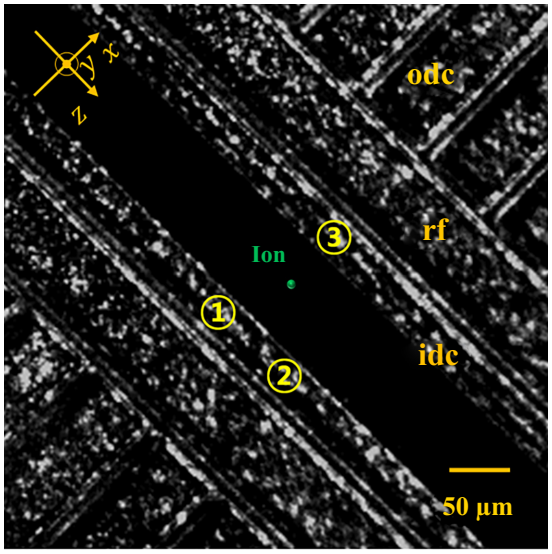

FIG. 8. CCD image of the surface-electrode ion trap in the vicinity of the trapped ion. Green dot indicates the initial ion position, and marks 1, 2, and 3 show laser-irradiation regions.

The following guidelines and tips are recommended for estimating the locations of laser-induced stray charges. First, it is suggested to measure the secular frequency shift by uniformly moving the ion along the z axis until the spacing between the ion and the nearest electrode is reached. If the frequency shift approaches zero near where z_{ion} approximately equals the ion-electrode spacing and a peak in the plot of secular frequency shift is observed, curve fitting can be performed. However, if the frequency shift does not approach zero, additional measurements may be required by moving the ion further along the z axis. To perform the curve fitting, it is necessary to obtain measurement results at different ion positions at least 3 times more than the expected number of stray-charge locations.

TABLE I. Estimated values from measured $\Delta\omega_z$ and the coordinates of laser-irradiation regions. Cases 1, 2, and 3 indicate the results when the laser irradiates marks 1, 2, and 3 in Fig. 8, respectively. Estimated values indicate the estimated results in the curve fitting, and the actual values mean the identified coordinates of laser-irradiation regions. The actual amount of produced charges cannot be obtained, and therefore, the actual Q is presented as (–). The units of x_q and z_q are μm, and the unit of Q is e.

	Estimated values			Actual values		
	x_q	z_q	Q	x_q	z_q	Q
Case 1	-47 ± 26	-25 ± 11	-277 ± 64	-51 ± 6	-23 ± 5	–
Case 2	-66 ± 31	47 ± 18	-489 ± 78	-54 ± 3	49 ± 3	–
Case 3	51 ± 14	-4 ± 9	-86 ± 2	59 ± 3	-5 ± 3	–

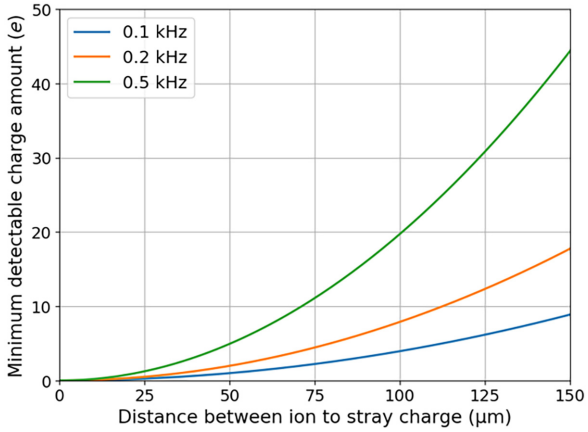

FIG. 9. Minimum detectable charge amount as a function of the distance between the ion and stray charge, represented as the absolute value. Minimum detectable charge amount is plotted against the accuracy of the secular frequency measurement, as indicated by blue, orange, and green lines for accuracies of 0.1, 0.2, and 0.5 kHz, respectively.

To evaluate the sensitivity of the proposed method for estimating the locations of stray charges, the relationship between the charge amount and the ion-to-stray-charge distance is investigated while varying the accuracy of the secular frequency measurement. The sensitivity depends on several factors, including the initial secular frequency, the ion-to-stray-charge distance, the charge amount, and the accuracy of the secular frequency measurement, as described by Eq. (9). In our investigation, we assume the initial secular frequency to be $2\pi \times 250$ kHz, which is the value used in the experiment, and vary the accuracy of the secular frequency measurement as $2\pi \times (0.1, 0.2, 0.5)$ kHz. The results are shown in Fig. 9, where the x axis represents the distance between the ion and the stray charge, ranging from 0 to 150 μm, and the y axis represents the absolute amount of charge, ranging from 0 to $50e$. The lines on the graph indicate the minimum amount of charge that can be detected by the secular frequency shift under the corresponding distance and frequency measurement accuracy. For example, based on our experimental results with 0.2-kHz accuracy, a stray charge as low as approximately $10e$ can be detected when the ion-to-stray-charge distance is approximately 115 μm, which corresponds to the distance between the ion and the nearest electrode in our trap. On the other hand, when the charge amount is $100e$, the stray charge up to approximately 350 μm away from the ion can be observed with an accuracy of 0.2 kHz.

In the process of estimating the fitting parameters, the margin of error for x_q is the largest among the fitting parameters. According to Eq. (9), since the calculation of x_q is carried out in the form of a square, the margin of error for x_q may be larger than that of z_q. The margin of error for z_q is smaller; however, the estimated margin of error is 10–20 μm. Additionally, the margin of error for Q is calculated to be a level of several to tens of electrons. The margin of error can be reduced by compensating for $\omega_{z0}(z_{\mathrm{ion}})$. The dc voltages are simulated and applied, and the residual micromotion is then canceled out by slightly adjusting the dc voltages. However, the ion position can be shifted in this process, and $\omega_{z0}(z_{\mathrm{ion}})$ can also be distorted. In the experiment, when the ion is located at the farthest point from $z_{\mathrm{ion}} = 0$, ω_{z0} decreases by approximately 22% compared with that of $z_{\mathrm{ion}} = 0$. By compensating for $\omega_{z0}(z_{\mathrm{ion}})$ at each ion position, the estimated margins of error for x_q, z_q, and Q in case 1 are reduced to 11 μm, 5 μm, and $31e$, respectively. The corrected margin of error is approximately half of what it is before the compensation. Also, the margin of error can be reduced if the measurement of secular frequency is more accurate. In the experiment, the margin of error for the secular frequency measurement is approximately 0.2 kHz, corresponding to 1.48 V/m of electric field and 0.35 μm of ion displacement in the surface-electrode ion trap. This measurement accuracy is comparable to the micromotion compensation techniques, which can detect electric fields of 1−5 V/m [21,22]. Instead of the parametric excitation method that can accompany electrical noise, other ways, such as the resolved sideband method [40], may reduce the measurement error.

This study assumes point charges for the simplicity of the model. However, when stray charges are induced by a laser, they can occur over an area with relatively large dimensions compared to the distance to the ion position. Also, when it is generated on top of the thin native oxide layer of the electrode material, the additional potential generated by the stray charge might behave close to that of the dipole moment rather than a point charge, depending on the geometry. We confirm that our method can still predict the center position of the charged area for different scenarios, even though the estimated amount of charge can vary by more than an order of magnitude. Additional details regarding this topic can be found in Appendix B.

A major disadvantage of the developed method is its relatively slow speed compared to the micromotion compensation techniques [24,36], as it involves scanning the frequency. In particular, the measurement speed is determined by the precision of the secular frequency measurement. However, this technique is still a useful tool to identify the locations of laser-induced stray charges, which can allow us to efficiently optimize the laser-propagation paths to reduce the occurrence of stray charges in surface-electrode ion traps.

V. CONCLUSIONS

We develop a method for estimating the locations of laser-induced stray charges on surface-electrode ion traps.

The variation in the electric potential at the trapped-ion location is modeled in the presence of a laser-induced stray charge, and the magnitude of the shift in the secular frequency of the trapped ion is derived from the model. Then, constraints are assumed to uniquely determine the location of stray charges from the secular frequency shift. In detail, it is assumed that the secular frequency can be measured at multiple ion positions in surface-electrode ion traps, and therefore, the required number of secular-frequency-shift measurements can be performed to determine the stray-charge locations uniquely. The model is then extended to the case where stray charges occur at multiple locations. Numerous test data are generated with the assumption of multiple stray charges at random locations, and the locations of multiple stray charges are estimated from the secular frequency shift observed in the test data. The estimated locations are then compared with the actual locations used to generate the test data. The number of stray-charge locations that can be distinguished using the developed method is also analyzed in this process. When different stray charges are sufficiently far apart enough to show different secular-frequency-shift peaks, locations of different stray charges can be easily estimated. However, when different stray charges are closely located and show a single peak, up to three charge locations can be identified. The effectiveness of the developed method is supported by simulating the effect of stray charges and by analyzing the resulting secular frequency shift. The locations of multiple stray charges are estimated from the secular frequency shift observed at multiple ion positions in the simulation. Also, experiments are performed to evaluate the developed method by intentionally producing electric charges at a single location by irradiating the laser onto that spot. The resulting secular frequency shift of the trapped ion is measured at multiple ion positions, and the location of produced charges is estimated from the measurement result. The estimated location of produced charges agrees with where the laser is irradiating within the margin of error. The developed method can be used to characterize laser-induced stray charges when trapped ions detect stray electric fields. This can be extended to designing experiments to avoid or reduce the occurrence of stray charges.

ACKNOWLEDGMENTS

All the authors are supported by the Samsung Research Funding & Incubation Center of Samsung Electronics under Project No. SRFC-IT1901-09. S.Y. and T.K. are additionally supported by a National Research Foundation of Korea (NRF) grant funded by the Korean Government (MSIT) under Project No. 2020M3E4A1079867.

APPENDIX A: CHARGE-DISSIPATION ANALYSIS

In this study, the secular frequency shift of a trapped ion is investigated while irradiating the electrode surface of the ion trap with a 399-nm laser. The secular frequency returns to its original value within 1 min after blocking laser irradiation, which is different from what is observed in other studies [25,31]. However, when irradiating the same spot with a 369.5-nm laser, the secular frequency does not return to its initial value for over 20 min after blocking the laser delivery, as depicted in Fig. 10. According to the model for the photoelectric effect on the oxidized electrode [26], when using the 369.5-nm laser, the kinetic energy of photoelectrons will be relatively high, and therefore, we conjecture that the photoelectrons may be trapped deep in the native oxide film, which leads to the observed slow rate of charge dissipation. Note that the measurement of secular frequency is challenging while delivering the 369.5-nm laser, since the reflected light from the electrode surface is strong. Additionally, using a 935-nm laser at the same region on the electrode surface does not change the secular frequency. Based on these results, the observed effect with the 399-nm laser is also attributed to the charging phenomenon caused by the laser on the oxidized electrode surface, despite the quick charge dissipation with the 399-nm laser in the experiment.

APPENDIX B: DIPOLE MODEL

When establishing the theoretical model, it is assumed that there is a point charge in free space, as discussed at the end of Sec. IV C. However, to demonstrate the practicality of the developed model even under other scenarios, a uniform charge density is assigned to an area of $10 \times 10\ \mu m^2$ using a COMSOL simulation, and then the secular frequency shift in the simulation and the charge amount estimated from the theoretical model are analyzed. Similar to the simulation conditions in Fig. 4, a surface charge density of $-10e/\mu m^2$ is applied to create a total charge of $-1000e$,

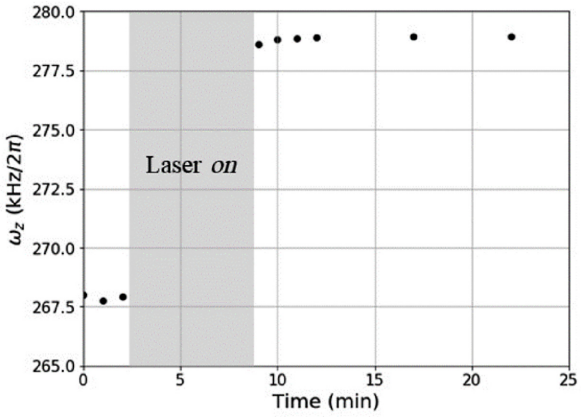

FIG. 10. Measurement result of secular frequency (ω_z) with the 369.5-nm laser. Gray box indicates the time while irradiating the electrode surface with the laser. Due to reflected light from the electrode surface, the secular frequency cannot be obtained in the gray box.

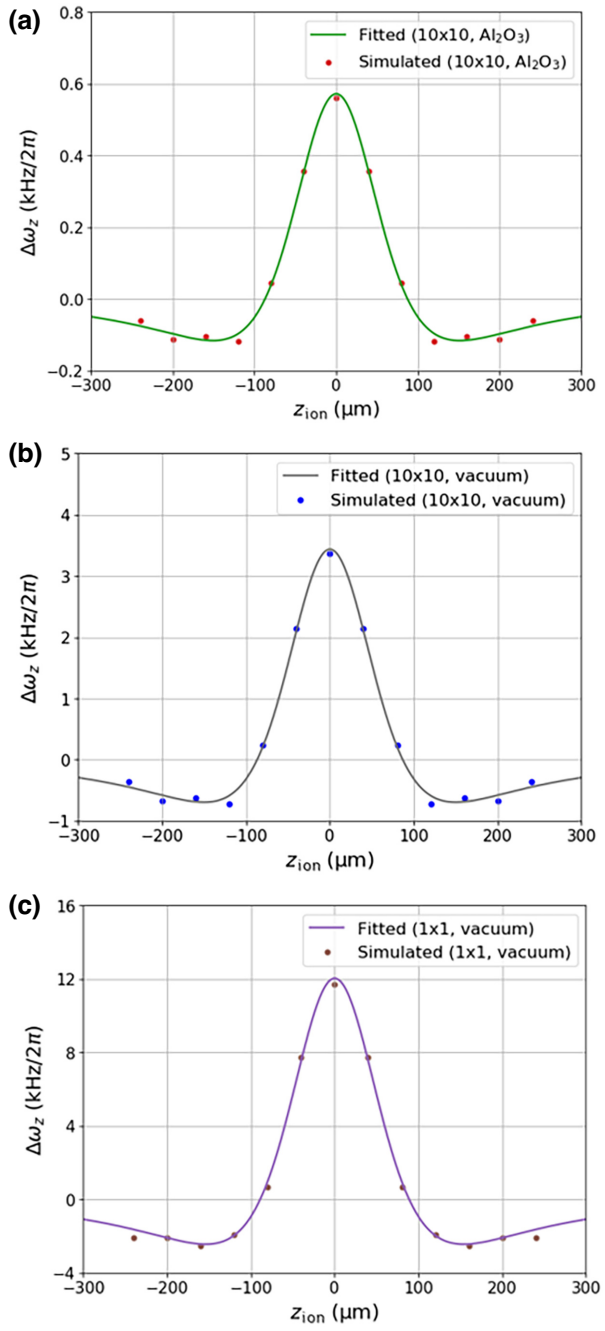

FIG. 11. Curve fitting and simulation results of $\Delta\omega_z$ as a function of z_{ion} for different scenarios, including varying surface charge densities, areas, and materials. (a) Surface charge density of $-10e/\mu m^2$ on an alumina area of 10×10 μm^2. (b) Surface charge density of $-10e/\mu m^2$ on an area of 10×10 μm^2 in a vacuum. (c) Surface charge density of $-1000e/\mu m^2$ on an area of 1×1 μm^2 in a vacuum. Corresponding fitting results are summarized in Table II.

and the center position of the charged area is set to (55, −108, 0) μm. The material beneath the induced charging area is assumed to be alumina (Al_2O_3), a native oxide film on an aluminum electrode, while the electrode itself is assumed to be grounded. The secular frequency shift is estimated by varying the distance between the ion and the charged region at intervals of 40 μm in the range of −240 to +240 μm along the z axis. As shown in Fig. 11(a), the magnitude of the secular frequency shift decreases by approximately 35 times, and the estimated charge amount obtained through curve fitting also decreases by approximately 36 times, resulting in a value of $-27e$. However, the estimated charge location is $(x_q, z_q) = (60,\ 0)\ \mu$m, which is comparable to the result obtained using a point charge within 7% error.

TABLE II. Summary of curve-fitting results shown in Fig. 11. 10×10 and 1×1 indicate the sizes of charged regions in μm^2, and the point represents a point charge. Surface charge density (ρ_s) denotes the magnitude of assigned charge density at the charged regions. The estimated location of the charge is indicated by $(x_q,\ z_q)$, and the estimated amount of charge is represented by Q. For all simulation results, the total charge amount is assumed to be $-1000e$, and y_q is assumed to be −108 μm.

Simulation condition	ρ_s ($e/\mu m^2$)	(x_q, z_q) (μm)	Q (e)
10×10 (Al_2O_3)	−10	(60, 0)	−27
10×10 (vacuum)	−10	(58, 0)	−159
1×1 (vacuum)	−1000	(63, 0)	−583
Point (vacuum)	–	(64, 0)	−979

As depicted in Figs. 11(b) and 11(c), similar simulations are conducted by changing the area and material underneath the induced surface charge density. The total amount of charge is set to be $-1000e$ for all cases, and the corresponding results are summarized in Table II. Although the area and the material are different, a similar shape of plot is observed, and then all the estimated location of stray charge is comparable. However, the estimated total charge amount has a large discrepancy, depending on the area and the material. Different dielectric constants may lead to different magnitudes of electric field inside the insulating film, resulting in different electric field gradients at the ion position. Also, a larger area results in a lower electric field gradient at the ion position, leading to a lower secular frequency shift, when the total charge amount is constant. Note that the main purpose of our study is to identify the location of stray charges and to extend our approach to estimate the relatively accurate amount of stray charges as well; a more elaborate model and information about the layer structure are required.

[1] B. Lekitsch, S. Weidt, A. G. Fowler, K. Molmer, S. J. Devitt, C. Wunderlich, and W. K. Hensinger, Blueprint for a microwave trapped ion quantum computer, Sci. Adv. **3,** e1601540 (2017).

[2] K. Wright, *et al.*, Benchmarking an 11-qubit quantum computer, Nat. Commun. **10,** 5464 (2019).

[3] J. M. Pino, J. M. Dreiling, C. Figgatt, J. P. Gaebler, S. A. Moses, M. S. Allman, C. H. Baldwin, M. Foss-Feig, D. Hayes, K. Mayer, C. Ryan-Anderson, and B. Neyenhuis, Demonstration of the trapped-ion quantum CCD computer architecture, Nature **592**, 209 (2021).

[4] D. Cho, S. Hong, M. Lee, and T. Kim, A review of silicon microfabricated ion traps for quantum information processing, Micro Nano Syst. Lett. **3**, 1 (2015).

[5] S. Auchter, C. Axline, C. Decaroli, M. Valentini, L. Purwin, R. Oswald, R. Matt, E. Aschauer, Y. Colombe, P. Holz, T. Monz, R. Blatt, P. Schindler, C. Rossler, and J. Home, Industrially microfabricated ion trap with 1 eV trap depth, Quantum Sci. Techhnol. **7**, 035015 (2022).

[6] S. Debnath, N. M. Linke, C. Figgatt, K. A. Landsman, K. Wright, and C. Monroe, Demonstration of a small programmable quantum computer with atomic qubits, Nature **536**, 63 (2016).

[7] N. H. Nguyen, M. Li, A. M. Green, C. H. Alderete, Y. Zhu, D. Zhu, K. R. Brown, and N. M. Linke, Demonstration of Shor Encoding on a Trapped-Ion Quantum Computer, Phys. Rev. Appl. **16**, 024057 (2021).

[8] D. Kielpinski, C. Monroe, and D. J. Wineland, Architecture for a large-scale ion-trap quantum computer, Nature **417**, 709 (2002).

[9] M. Lee, J. Jeong, Y. Park, C. Jung, T. Kim, and D. Cho, Ion shuttling method for long-range shuttling of trapped ions in MEMS-fabricated ion traps, Jap. J. Appl. Phys. **60**, 027004 (2021).

[10] M. Lee, M. Lee, S. Hong, K. Schuppert, Y.-D. Kwon, T. Kim, Y. Colombe, T. E. Northup, D. Cho, and R. Blatt, Microelectromechanical-System-Based Design of a High-Finesse Fiber Cavity Integrated with an Ion Trap, Phys. Rev. Appl. **12**, 044052 (2019).

[11] K. K. Mehta, C. Zhang, M. Malinowski, T.-L. Nguyen, M. Stadler, and J. P. Home, Integrated optical multi-ion quantum logic, Nature **586**, 533 (2020).

[12] D. T. C. Allcock, T. P. Harty, C. J. Balance, B. C. Keitch, N. M. Linke, D. N. Stacey, and D. M. Lucas, A microfabricated ion trap with integrated microwave circuitry, Appl. Phys. Lett. **102**, 044103 (2013).

[13] N. D. Guise, S. D. Fallek, K. E. Stevens, K. R. Brown, C. Volin, A. W. Harter, J. M. Amini, R. E. Higashi, S. T. Lu, H. M. Chanhvongsak, T. A. Nguyen, M. S. Marcus, T. R. Ohnstein, and D. W. Youngner, Ball-grid array architecture for microfabricated ion traps, J. Appl. Phys. **117**, 174901 (2015).

[14] M. Siegele-Brown, S. Hong, F. R. Lebrun-Gallagher, S. J. Hile, S. Weidt, and W. K. Hensinger, Fabrication of surface ion traps with integrated current carrying wires enabling high magnetic field gradients, Quantum Sci. Technol. **7**, 034003 (2022).

[15] M. Brownnutt, M. Kumph, P. Rabl, and R. Blatt, Ion-trap measurements of electric-field noise near surfaces, Rev. Mod. Phys. **87**, 1419 (2015).

[16] F. R. Ong, K. Schuppert, P. Jobez, M. Teller, B. Ames, D. A. Fioretto, K. Friebe, M. Lee, Y. Colombe, R. Blatt, and T. E. Northup, Probing surface charge densities on optical fibers with a trapped ion, New J. Phys. **22**, 063018 (2020).

[17] C. J. Balance, T. P. Harty, N. M. Linke, M. A. Sepiol, and D. M. Lucas, High-Fidelity Quantum Logic Gates Using Trapped-Ion Hyperfine Qubits, Phys. Rev. Lett. **117**, 060504 (2016).

[18] J. Keller, D. Kalincev, T. Burgermeister, A. P. Kulosa, A. Didier, T. Nordmann, J. Kiethe, and T. E. Mehlstäubler, Probing Time Dilation in Coulomb Crystals in a High-Precision Ion Trap, Phys. Rev. Appl. **11**, 011002 (2019).

[19] S. Hong, Y. Kwon, C. Jung, M. Lee, T. Kim, and D. Cho, A new microfabrication method for ion-trap chips to reduce exposed dielectric surfaces from trapped ions, J. Microelectromech. Syst. **27**, 28 (2017).

[20] Z. D. Romaszko, S. Hong, M. Siegele, R. K. Puddy, F. R. Lebrun-Gallagher, S. Weidt, and W. K. Hensinger, Engineering of microfabricated ion traps and integration of advanced on-chip features, Nat. Rev. Phys. **2**, 285 (2020).

[21] D. T. C. Allcock, J. A. Sherman, D. N. Stacey, A. H. Burrell, M. J. Curtis, G. Imreh, N. M. Linke, D. J. Szwer, S. C. Webster, A. M. Steane, and D. M. Lucas, Implementation of a symmetric surface-electrode ion trap with field compensation using a modulated Raman effect, New J. Phys. **12**, 053026 (2010).

[22] S. Narayanan, N. Daniilidis, S. A. Moller, R. Clark, F. Ziesel, K. Singer, F. Schmidt-Kaler, and H. Haffner, Electric field compensation and sensing with a single ion in a planar trap, J. Appl. Phys. **110**, 114909 (2011).

[23] R. Saito, K. Saito, and T. Mukaiyama, Measurement of ion displacement via rf power variation for excess micromotion compensation, J. Appl. Phys. **129**, 124302 (2021).

[24] L. A. Zhukas, M. J. Millican, P. Svihra, A. Nomerotski, and B. B. Blinov, Direct observation of ion micromotion in a linear Paul trap, Phys. Rev. A **103**, 023105 (2021).

[25] M. Harlander, M. Brownnutt, W. Hansel, and R. Blatt, Trapped-ion probing of light-induced charging effects on dielectrics, New J. Phys. **12**, 093035 (2010).

[26] S. X. Wang, G. H. Low, N. S. Lachenmyer, Y. Ge, P. F. Herskind, and I. L. Chuang, Laser-induced charging of microfabricated ion traps, J. Appl. Phys. **110**, 104901 (2011).

[27] C. Jung, W. Lee, J. Jeong, M. Lee, Y. Park, T. Kim, and D. Cho, A microfabricated ion trap chip with a sloped loading slot to minimize exposing trapped ions to stray charges, Quantum Sci. Technol. **6**, 044004 (2021).

[28] A. Harter, A. Krukow, A. Brunner, and J. H. Denschlag, Long-term drifts of stray electric fields in a Paul trap, Appl. Phys. B **114**, 275 (2014).

[29] C. D. Bruzewicz, J. Chiaverini, R. McConnell, and J. M. Sage, Trapped-ion quantum computing: Progress and challenges, Appl. Phys. Rev. **6**, 021314 (2019).

[30] N. P. de Leon, K. M. Itoh, D. Kim, K. K. Mehta, T. E. Northup, H. Paik, B. S. Palmer, N. Samarth, S. Sangtawesin, and D. W. Steuerman, Materials challenges and opportunities for quantum computing hardware, Science **372**, eabb2823 (2021).

[31] D. T. C. Allcock, T. P. Harty, H. A. Janacek, N. M. Linke, C. J. Balance, A. M. Steane, D. M. Lucas, R. L. Jarecki Jr, S. D. Habermehl, M. G. Blain, D. Stick, and D. L. Moehring, Heating rate and electrode charging measurements in a scalable microfabricated, surface-electrode ion trap, Appl. Phys. B **107**, 913 (2012).

[32] S. C. Doret, J. M. Amini, K. Wright, C. Volin, T. Killian, A. Ozakin, D. Dension, H. Hayden, C.-S. Pai, R. E. Slusher, and A. W. Harter, Controlling trapping potentials and stray electric fields in a microfabricated ion trap through design and compensation, New J. Phys. **14**, 073012 (2012).

[33] P. C. Holz, S. Auchter, G. Stocker, M. Valentini, K. Lakhmanskiy, C. Rossler, P. Stampfer, S. Sgouridis, E. Aschauer, Y. Colombe, and R. Blatt, 2D linear trap array for quantum information processing, Adv. Quantum Technol. **3**, 2000031 (2020).

[34] S. Hong, M. Lee, Y. Kwon, D. Cho, and T. Kim, Experimental methods for trapping ions using microfabricated surface ion traps, J. Visualized Exp. **126**, e56060 (2017).

[35] W. Paul, H. P. Reinhard, and U. Von Zahn, Das elektrische Massenfilter als Massenspektrometer und Isotopentrenner, Z. Phys. **152**, 143 (1958).

[36] D. Leibfried, R. Blatt, C. Monroe, and D. Wineland, Quantum dynamics of single trapped ions, Rev. Mod. Phys. **75**, 281 (2003).

[37] P. Virtanen, *et al.*, SciPy 1.0: Fundamental algorithms for scientific computing in PYTHON, Nat. Methods **17**, 261 (2020).

[38] S. Menezes, R. Haak, G. Hagen, and M. Kendig, Photoelectrochemical characterization of corrosion inhibiting oxide films on aluminum and its alloy, J. Electrochem. Soc. **136**, 1884 (1989).

[39] Y. Ibaraki, U. Tanaka, and S. Urabe, Detection of parametric resonance of trapped ions for micromotion compensation, Appl. Phys. B **105**, 219 (2011).

[40] C. Monroe, D. M. Meekhof, B. E. King, S. R. Jefferts, W. M. Itano, D. J. Wineland, and P. Gould, Resolved-Sideband Raman Cooling of a Bound Atom to the 3D Zero-Point Energy, Phys. Rev. Lett. **75**, 4011 (1995).